Supplementary Information of

Orpiment under compression: metavalent bonding at high pressure

V.P. Cuenca-Gotor,[1] J.A. Sans,[1,] O. Gomis,[2] A. Mujica,[3] S. Radescu,[3] A. Muñoz,[3] P. Rodríguez-Hernández,[3] E. Lora da Silva,[1] C. Popescu,[4] J. Ibañez,[5] R. Vilaplana,[2] and F.J. Manjón[1,*]*

[1] Instituto de Diseño para la Fabricación y Producción Automatizada, Universitat Politècnica de València, 46022 Valencia (Spain)

[2] Centro de Tecnologías Físicas, Universitat Politècnica de València, 46022 Valencia (Spain)

[3] Departamento de Física, Instituto de Materiales y Nanotecnología, MALTA Consolider Team, Universidad de La Laguna, 38207 San Cristóbal de La Laguna (Spain)

[4] ALBA-CELLS, 08290 Cerdanyola, Barcelona (Spain)

[5] Institute of Earth Sciences Jaume Almera, CSIC, 08028 Barcelona (Spain)

Structural properties of orpiment at room conditions

Table S1. Theoretical (the, with vdW) and experimental (exp) atomic parameters of the $P2_1/c$ structure of α-As_2S_3 at room conditions.

Atoms	Site	x	Y	z
As1	*4e*	0.10723 (the) [a] 0.09805 (exp)[b]	0.30752 (the) [a] 0.30829 (exp)[b]	0.23420 (the) [a] 0.23531 (exp) [b]
As2	*4e*	0.38070 (the) [a] 0.37395 (exp) [b]	0.17785 (the) [a] 0.17878 (exp) [b]	0.01176 (the) [a] 0.01323 (exp) [b]
S1	*4e*	0.61732 (the) [a] 0.60660 (exp) [b]	0.37901 (the) [a] 0.37872 (exp)[b]	0.09901 (the) [a] 0.09849 (exp) [b]
S2	*4e*	0.1719 (the) [a] 0.16272 (exp) [b]	0.0999 (the) [a] 0.10277 (exp) [b]	0.15133 (the) [a] 0.15262 (exp) [b]
S3	*4e*	0.05703 (the) [a] 0.06338 (exp) [b]	0.70532 (the) [a] 0.70646 (exp) [b]	0.12304 (the) [a] 0.12234 (exp)[b]

[a] This work. [b] Data from Ref. 1 converted with VESTA from the original $P2_1/n$ setting to the standard $P2_1/c$ setting with coordinate standardization.

Vibrational properties of orpiment at room conditions

Group theory predicts sixty zone-center vibrational modes at the BZ center for α-As_2S_3 with mechanical representation **[2]**:

$$\Gamma_{60} = 15\ (A_g(R) + B_u\ (IR)) + 15\ (B_g\ (R) + A_u\ (IR)) \quad (1)$$

where g (gerade) modes are Raman-active (R) and u (ungerade) modes are infrared-active (IR). Note that all modes are paired up, (A_g,B_u) and (B_g,A_u), where the first is R and the second is IR. Therefore, α-As_2S_3 has 30 Raman-active modes and 27 IR-active modes because one A_u and two B_u modes are acoustic modes. A_g and B_u modes correspond mainly to vibrations of atoms in the *ac*-plane, while B_g and A_u modes correspond mainly to atomic vibrations along the *b*-axis.

It is well-known that in layered materials with layers piled along the *c*-axis, which usually crystallize either in a hexagonal or tetragonal space groups, the lowest-frequency E (doubly degenerated) and A (or B) modes at the Γ-point can be classified as inter-layer modes (out-of-phase vibrations of atoms corresponding to adjacent layers), also known as rigid layer modes, or intra-layer modes (out-of-phase vibrations of atoms inside the layers) **[3]**. Inter-layer E and A (or B) modes are usually related to shear or transversal vibrations between adjacent layers along the *a*- or *b*-direction of the *ab*-layer plane and to longitudinal vibrations of one layer against the adjacent ones (along the *c*-axis), respectively.

Both E and A (or B) inter-layer modes arise from the transverse acoustic (TA) and longitudinal acoustic (LA) modes, respectively, due to the band folding of the Brillouin zone boundaries into the Γ-point due to the decrease of symmetry from cubic to hexagonal or tetragonal. Similarly, E and A (or B) intra-layer modes originate from the transverse optical (TO) and longitudinal optical (LO) modes at Γ-point and from additional modes due to the folding of the BZ boundaries into the Γ-point **[3]**.

The number of inter-layer and intra-layer modes in layered materials depends on the complexity of the unit cell. In the simplest case, there should be two inter-layer modes and four intra-layer modes. For α-As_2S_3, which crystallizes on the monoclinic phase, there are only modes with A and B symmetry, therefore there are three inter-layer rigid modes. Since the acoustic modes are one A_u and two B_u modes, corresponding to inter-layer rigid modes where both layers of the unit cell have in-phase translations, the out-of-phase translations of the two layers corresponding to the three optical inter-layer rigid modes must be Raman-active and must be two A_g and one B_g modes. We have visualized the atomic motions of the normal vibrations of α-As_2S_3 with the use of J-ICE program **[4]**. Two of these are the two shear rigid modes with lowest-frequency (27 and 389 cm^{-1}) represented in **Figure S1** and that are attributed to the A_g^1 and A_g^2 modes as indicated in previous papers (see **Ref. 1** and references therein). On the other hand, the

compressional or longitudinal rigid mode is the B_g^1 mode located around 62 cm^{-1} (see **Figure S2**). As commented in previous papers, this compressional rigid mode has a similar frequency to other optical modes; i.e. there is a mix between this inter-layer mode and several inter-chain modes (see **Figure S3**) as previously suggested **[2]**.

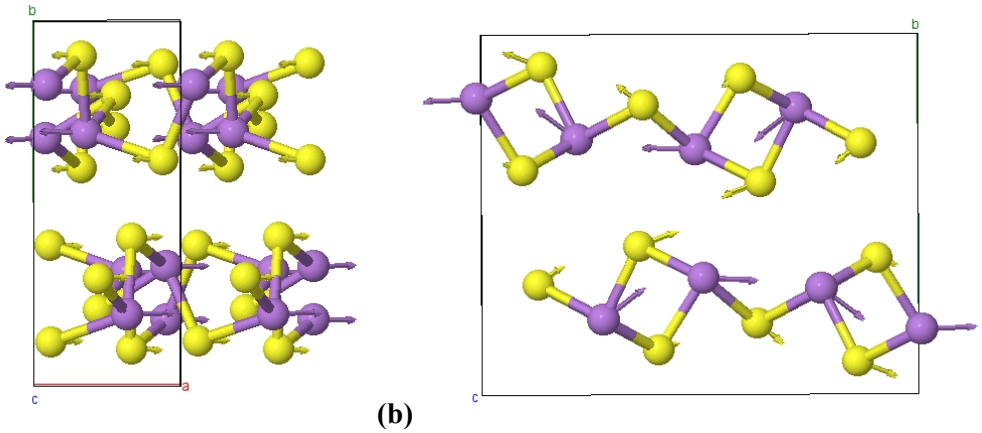

(a) **(b)**

Figure S1. Atomic vibrations of the A_g^1 **(a)** and A_g^2 **(b)** inter-layer modes located around 27 and 38 cm^{-1} in the *ab*- (*bc*)-plane. These are the shear rigid layer modes in α-As_2S_3. As: Purple spheres, S: yellow spheres.

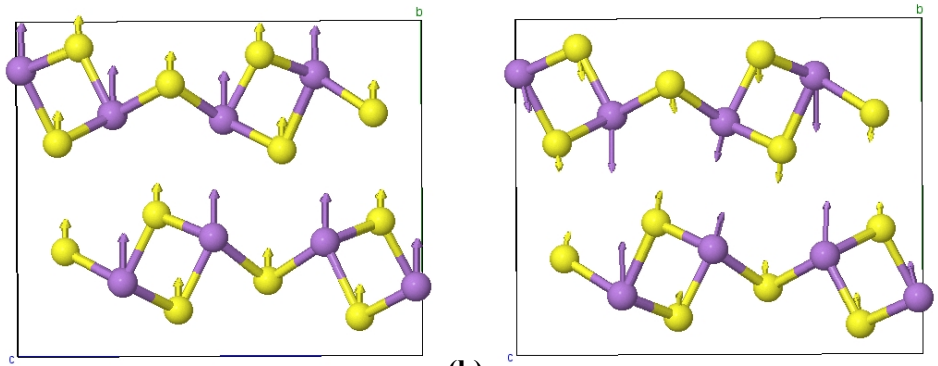

(a) **(b)**

Figure S2. Atomic vibrations of the acoustic A_u inter-layer mode **(a)** and the related B_g^1 inter-layer mode located around 62 cm^{-1} **(b)** in the *bc*-plane. The B_g^1 mode is the longitudinal or compressional rigid layer mode in α-As_2S_3. As: Purple spheres, S: yellow spheres.

Intra-layer modes can be divided into high-frequency intra-chain modes and low-frequency inter-chain modes **[2]**. The mixture of inter-layer and inter-chain modes found is in agreement with the analysis of Defonzo and Tauc **[2]**. In fact, low-frequency inter-chain modes mixed with the compressional rigid mode are those related to the rotation of the AsS spiral chains around the *a*-axis (see **Figures S3** and **S4**), and there are also modes related to the translation of the spiral chains inside each layer (see **Figures S5** to **S8**).

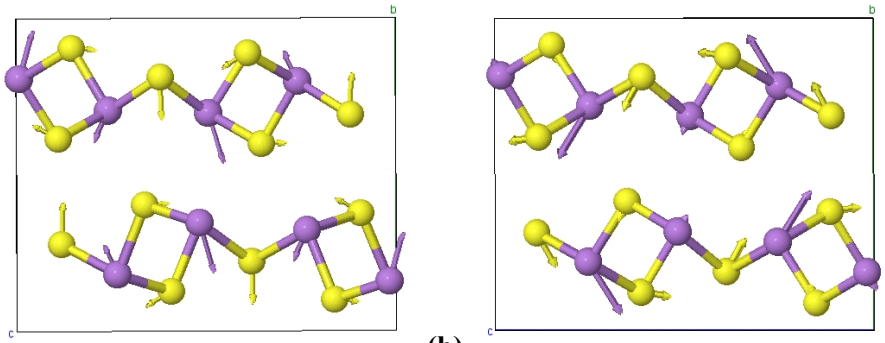

(a) **(b)**

Figure S3. Atomic vibrations of the B_u^1 **(a)** and A_g^3 **(b)** modes located around 50 and 59 cm^{-1}, respectively, in the *bc*-plane. These are inter-chain modes of α-As_2S_3 corresponding to rotational modes of the spiral AsS chains around the *a*-axis (perpendicular to the page). Atoms of one chain rotate around the *a*-axis in the opposite sense (clockwise vs. counter-clockwise) than the neighbour chains inside the same layer. Rotations of the neighbour chains in the adjacent layers are in the same direction in the B_u mode and in the opposite direction in the A_g mode. These are two of the "inter-chain rolling" modes defined in Ref. **[2]**. As: Purple spheres, S: yellow spheres.

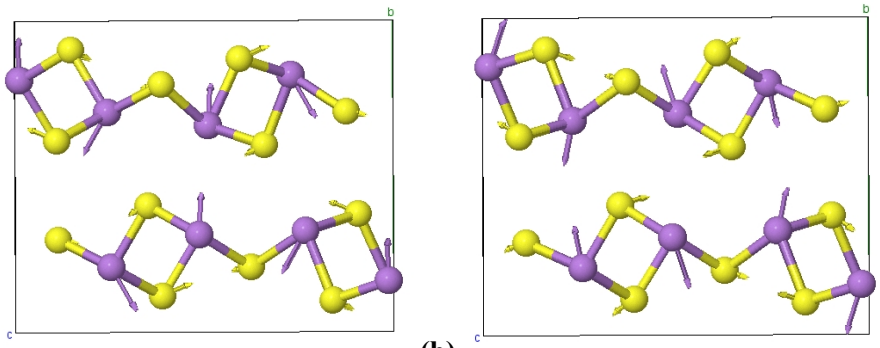

(a) **(b)**

Figure S4. Atomic vibrations of the A_u^2 mode **(a)** and the B_g^4 mode **(b)** located around 93 and 103 cm^{-1}, respectively, in the *bc*-plane. These are inter-chain modes corresponding to rotational modes of the AsS spiral chains around the *a*-axis. Atoms of one chain rotate around the *a*-axis in the same direction as the neighbour chains inside the same layer. Rotations of the chains in the adjacent layers are in opposite direction (clockwise vs. counterclockwise) in the A_u mode and in the same direction in the B_g mode. These are other two "inter-chain rolling" modes defined in Ref. **[2]**. As: Purple spheres, S: yellow spheres.

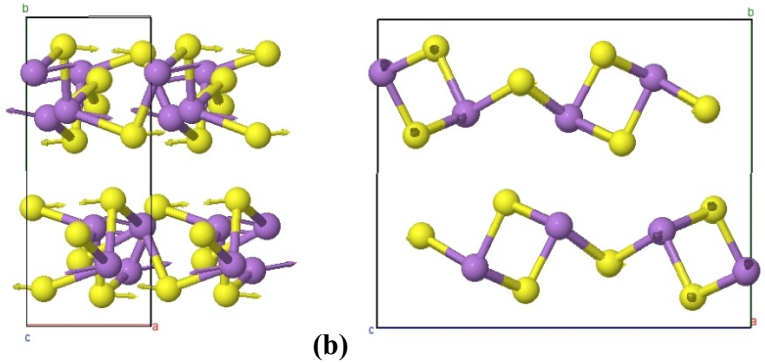

(a) **(b)**

Figure S5. Atomic vibrations of the mode A_g^4 located around 70 cm^{-1} in the *ba*- **(a)** and *bc*-planes **(b)**. This is an inter-chain mode corresponding to translations of the spiral chains along the *a*-axis. Atoms of one spiral chain translate along the *a*-axis in oposite phase with respect to those of the neighbour chains inside the same layer. Translations in the neighbour layers are opposite to those

of the first layer. The S atoms linking the chains (S3 atoms) are almost at rest. As: Purple spheres, S: yellow spheres.

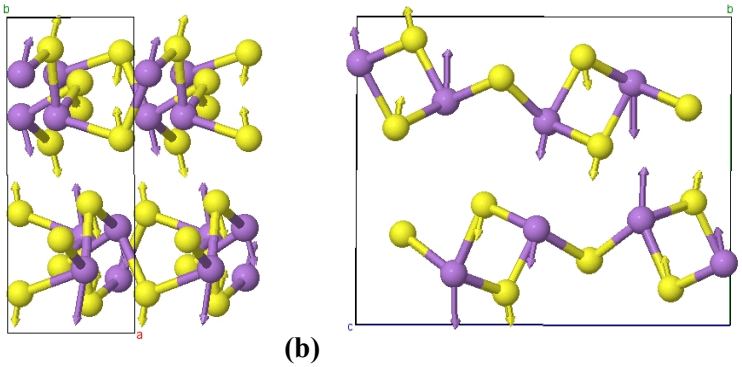

(a) **(b)**

Figure S6. Atomic vibrations of the A_u^1 mode located around 63 cm^{-1} in the *ba*- **(a)** and *bc*-planes **(b)**. This is an inter-chain mode corresponding to translations of the spiral chains mainly along the *b* axis, together with a minor rotation around the *a*-axis. Atoms of one chain translate in opposite phase with respect to those of the neighbour chains both in the same layer and in neighbour layers. The S atoms (S3) linking the chains are almost at rest. As: Purple spheres, S: yellow spheres.

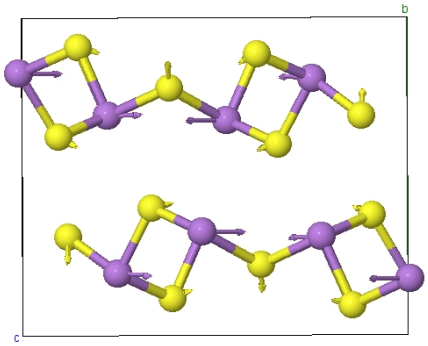

Figure S7. Atomic vibrations of the B_u^2 mode located around 94 cm^{-1} in the *bc* plane. This is an inter-chain mode corresponding to translations of the spiral chains along the *c*-axis. Atoms of one chain translate in opposite phase with respect to atoms of the neighbour chains in the same layer. This is the "inter-chain beating" mode of orpiment **[2]** and it is the pair of the A_g^4 mode around 70 cm^{-1}. As: Purple spheres, S: yellow spheres.

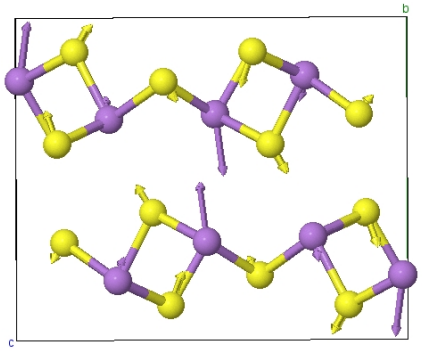

Figure S8. Atomic vibrations of the B_g^2 mode located around 69 cm^{-1} in the *bc*-plane. This is an inter-chain mode corresponding to a mixture of translations of the spiral chains mainly along the *b*-axis together with a small rotation around the *a*-axis. Atoms of one chain translate in opposite phase with respect to those of the neighbour chains in the same layer. The S atoms linking the

chains are almost at rest. This is the pair of the A_u^1 mode around 63 cm^{-1}. As: Purple spheres, S: yellow spheres.

Several modes located around 150 cm^{-1} are related to vibrations of the S3 atoms (outside the chains), which vibrate in a completely different manner to the S1 and S2 atoms (inside the chains). These modes evidence the chain-like nature of the layers (see **Figure S9**). Finally, it can be stressed that there are typical bending modes in the intermediate-frequency region (**Figure S10**), modes involving partial bending and stretching (**Figure S11**) and typical stretching modes in the high-frequency region (**Figures S12, S13, and S14**).

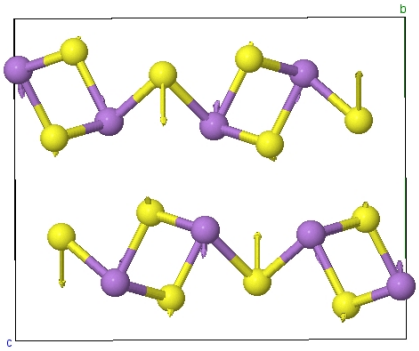

Figure S9. Atomic vibrations of the A_g^6 mode located at 153 cm^{-1} in the *bc* plane. This mode corresponds to an intra-layer mode mainly characterized by vibrations of the S atoms between the chains (S3 atoms).

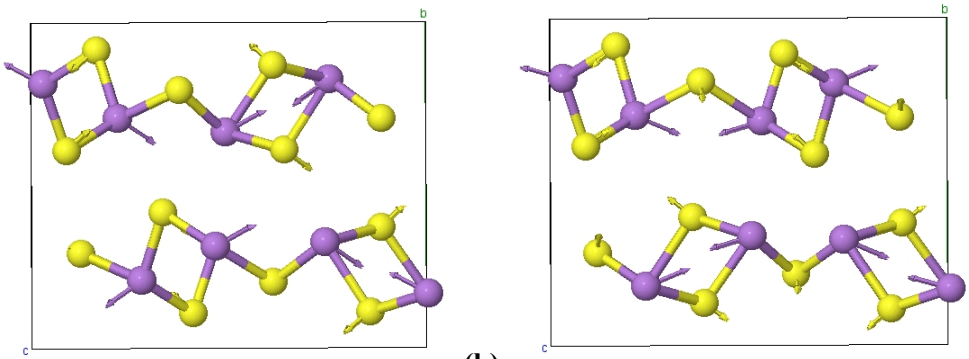

(a) **(b)**

Figure S10. Atomic vibrations of the A_u^7 mode (a) and B_u^7 mode (b) located at 167 and 196 cm^{-1}, respectively, in the *bc* plane. They correspond to intra-chain modes where atoms of a semi-rod vibrate in opposite phase against the other semi-rod. As: Purple spheres, S: yellow spheres.

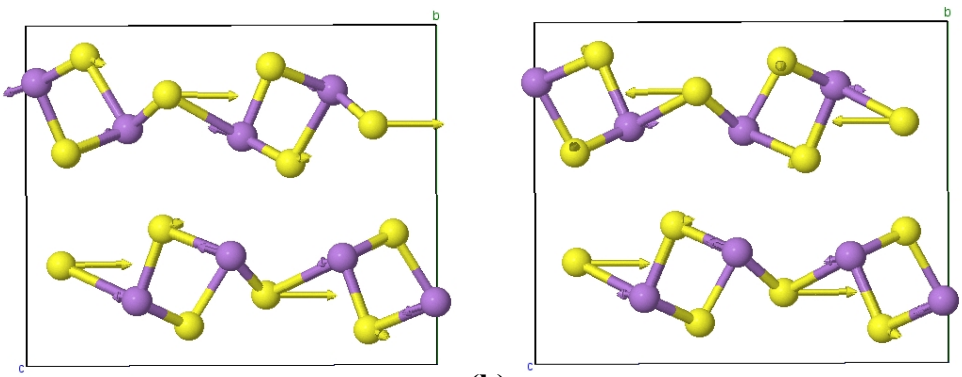

(a) **(b)**

Figure S11. Atomic vibrations of the B_u^8 mode (a) and the A_g^{10} mode (b) located around 269 and 270 cm^{-1}, respectively, in the *bc* plane. These high-frequency modes correspond to intra-layer modes mainly characterized by bending As-S vibrations. In particular, these two modes are related to vibrations of S3 atoms in the plane of the layers.

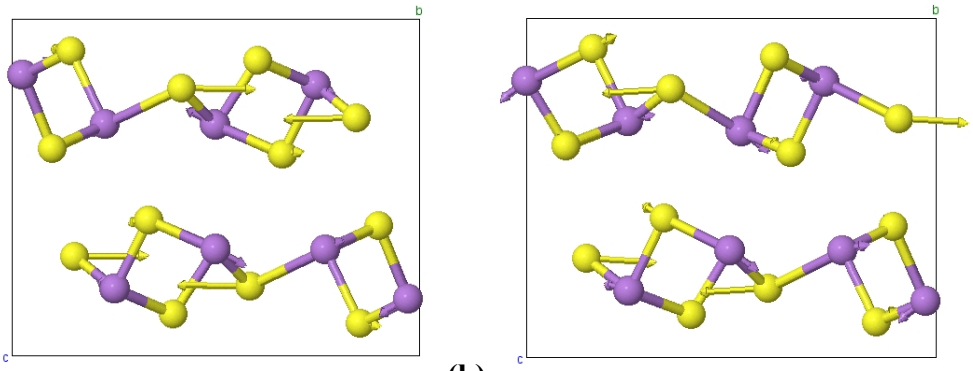

(a) **(b)**

Figure S12. Atomic vibrations of the B_g^{11} mode (a) and the A_u^{10} mode (b) located around 305 and 307 cm^{-1}, respectively, in the *bc* plane. These high-frequency modes correspond to intra-layer modes mainly characterized by bending As-S vibrations. In particular, these two modes are related to vibrations of S3 atoms in the plane of the layers.

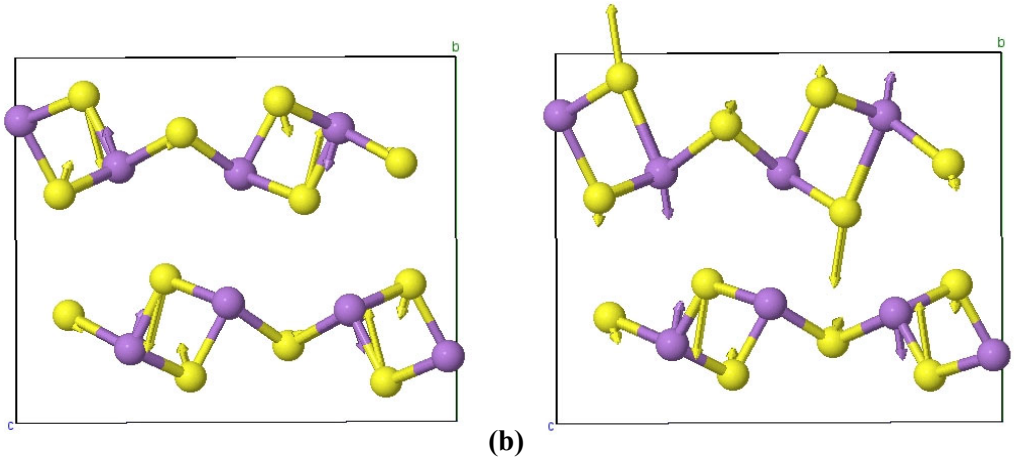

(a) **(b)**

Figure S13. Atomic vibrations of the A_g^{14} mode (a) and the B_u^{12} mode (b) located around 346 and 350 cm^{-1}, respectively, in the *bc* plane. These high-frequency modes correspond to intra-chain modes mainly characterized by symmetric stretching As-S vibrations. All vibrational modes around 340-350 cm^{-1} are characterized by similar symmetric stretching intra-chain As-S vibrations.

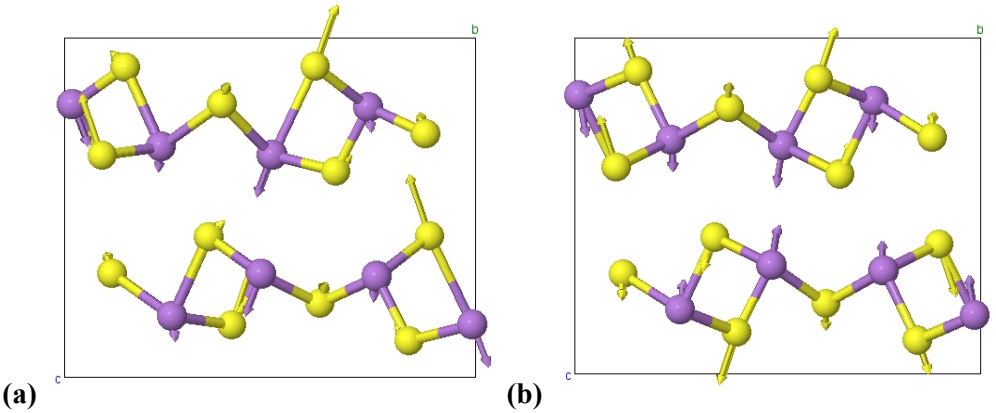

(a) **(b)**

Figure S14. Atomic vibrations of the A_u^{14} mode (a) and the B_g^{15} mode (b) located around 374 and 385 cm^{-1}, respectively, in the *bc* plane. These high-frequency modes correspond to intra-chain

modes mainly characterized by stretching As-S vibrations. All four vibrational modes located above 370 cm^{-1} are characterized by similar asymmetric stretching intra-chain As-S vibrations.

Structural properties of orpiment under high pressure

Calculation of the experimental and theoretical compressibility tensor at different pressures

The isothermal compressibility tensor, β_{ij}, is a symmetric second rank tensor that relates the state of strain of a crystal to the change in pressure that induced it **[5]**. The tensor coefficients for a monoclinic crystal with *b* as the unique crystallographic axis are:

$$\beta_{ij} = \begin{pmatrix} \beta_{11} & 0 & \beta_{13} \\ 0 & \beta_{22} & 0 \\ \beta_{13} & 0 & \beta_{33} \end{pmatrix}$$

We have obtained the isothermal compressibility tensor coefficients for monoclinic As_2S_3 at several pressures using the Institute of Radio Engineers (IRE) convention for the orthonormal basis for the tensor: $e_3||c, e_2||b^*, e_1||e_2 \times e_3$. The tensor has been obtained with the finite Eulerian approximation as implemented in the Win_Strain package **[6]**.

The change of the β monoclinic angle (always perpendicular to the *b*-axis) with pressure implies that, in this monoclinic compound, the direction of the *a*-axis changes with pressure assuming both *b*- and *c*-axis constant. Furthermore, the variation of this monoclinic angle from 90º indicates that the direction of maximum compressibility is not exactly that of the *a*-axis. Therefore, in order to evaluate the direction of maximum compressibility as a function of pressure, we have calculated and diagonalized the experimental and theoretical isothermal compressibility tensor, β_{ij}, at different pressures.

The experimental and theoretical elements of this tensor at different pressures are reported in Tables 1 and 2, up to 10.0 and 32.0 GPa, respectively, where the directions of the maximum, intermediate and minimum compressibility and the values of the compressibility along those directions are given by the eigenvectors (ev_i, i=1-3) and eigenvalues (λ_i, i=1-3), respectively.

First of all, we have to note that there is a reasonable good agreement between the experimental and calculated axial compressibilities (β_{ii} coefficients) at room pressure because $\beta_{11} \geq \beta_{22} > \beta_{33}$ in both cases. This result shows that the compressibility along the *a*-axis (layer plane) is greater or similar than that of the *b*-axis (axis perpendicular to the layer) and much larger than the *c*-axis. This is an unexpected result for a layered crystal whose layers extend in the *ac* plane and it is also a clear indication of the acicular (quasi-molecular) character of the layers.

Diagonalization of the β_{ij} tensor at room pressure yields for our experiments the maximum, intermediate and minimum compressibilities $36.4(1.8)\cdot10^{-3}$, $31.3(1.6)\cdot10^{-3}$ and $-0.7(3)\cdot10^{-3}$ GPa^{-1}, respectively; whereas for the case of our calculations the obtained values for the compressibilities are $44.7(2.4)\cdot10^{-3}$, $25.8(1.3)\cdot10^{-3}$ and $-1.14(15)\cdot10^{-3}$ GPa^{-1}. These experimental (theoretical) results indicate that around 48% (58%) of the total compression at room pressure is being accommodated along the direction of maximum compressibility. The direction of the maximum compressibility at zero pressure, given by the eigenvector ev_1, occurs at the (0 1 0) plane and it is defined by angle Ψ (see **Tables 1 and 2**) relative to the *c*-axis (from *c* to *a*) or equivalently by an angle θ relative to the *a*-axis (from *a* to *c*). The direction of intermediate compressibility at zero pressure, given by eigenvector ev_2, is along the *b*-axis. Finally, the direction of minimum compressibility at zero pressure, given by eigenvector ev_3, is at the (0 1 0) plane and perpendicular to the direction of maximum compressibility within the same plane. In particular, the experimental direction of maximum compressibility at room pressure is at θ =0.8(3)º from the *a*-axis, whereas the calculated one is at 1.12(20)º. This means that the direction of maximum (minimum) compressibility at room pressure is close to the *a*-axis (*c*-axis).

As regards the behaviour of the experimental (theoretical) compressibility tensor under pressure, we start with the study between 0 and 10 GPa where both the theoretical and experimental β_{ij} values have been obtained. The most notable feature is that $\beta_{11} \geq \beta_{22} > \beta_{33}$ is maintained as pressure increases. Therefore, our experiment (*ab initio* calculations) shows that the *a*-axis has compressibility greater or similar (greater) than that of the *b*-axis. In this sense, a greater or similar compressibility in a direction along the layer with respect to that of the inter-layer (along the *b*-axis) is maintained with compression. On the other hand, the eigenvalue λ_3 is negative below 0.9 (1.3) GPa in the case of the experimental (theoretical) β_{ij} tensor. This means that the material slightly expands under compression (positive strain) along the direction of minimum compressibility, given by the eigenvector ev_3. On the other hand, the direction of major compression is close to the *a*-axis under compression.

Above 10 GPa, the theoretical compressibility tensor has been obtained up to 32.0 GPa. In this case, the direction of maximum compressibility changes rapidly for pressures greater than 20 GPa. For instance, θ=46(13)º at 22.2 GPa and the direction of maximum compressibility is along the *b*-axis ([010] direction) at 24.3 GPa. However, the direction of maximum compressibility is again at the *ac* plane above 26.7 GPa, but it is close to the *c*-axis instead. In particular, Ψ = 15(4) and θ=92(4)º at 32.0 GPa.

Table 1. Experimental isothermal compressibility tensor coefficients, β_{ij}, for As_2S_3 and their respective eigenvalues, λ_i, and eigenvectors, ev_i, at different pressure values. The results are obtained by employing the finite Eulerian method. The eigenvalues are given in decreasing value along a column.

P(GPa)	0.0	1.0	2.0	3.0	4.0	5.0	6.0	8.0	10.0
β_{11} (10^{-3} GPa^{-1})	32.4(1.8)	23.0(1.2)	17.3(1.2)	14.0(1.0)	11.8(9)	10.2(7)	9.0(7)	7.4(6)	6.3(6)
β_{22} (10^{-3} GPa^{-1})	31.3(1.6)	21.2(1.1)	15.1(1.1)	11.8(0.8)	9.6(7)	8.2(6)	7.1(5)	5.6(4)	4.6(5)
β_{33} (10^{-3} GPa^{-1})	3.3(3)	3.2(3)	3.0(3)	2.9(3)	2.8(3)	2.8(3)	2.7(3)	2.5(3)	2.4(5)
β_{13} (10^{-3} GPa^{-1})	-11.5(5)	-8.4(4)	-6.0(4)	-4.5(3)	-3.5(3)	-2.84(23)	-2.31(20)	-1.51(15)	-0.94(22)
λ_1 (10^{-3} GPa^{-1})	36.4(1.8)	26.1(1.3)	19.5(1.4)	15.6(1.1)	13.0(9)	11.2(8)	9.8(7)	7.8(6)	6.6(6)
ev_1 (λ_1)	(0.94,0,-0.33)	(0.94,0,-0.34)	(0.94,0,-0.34)	(0.94,0,-0.34)	(0.94,0,-0.33)	(0.95,0,-0.32)	(0.95,0,-0.31)	(0.96,0,-0.27)	(0.98,0,-0.22)
λ_2 (10^{-3} GPa^{-1})	31.3(1.6)	21.2(1.1)	15.1(1.1)	11.8(8)	9.6(7)	8.2(6)	7.1(5)	5.6(4)	4.6(5)
ev_2 (λ_2)	(0,1,0)	(0,1,0)	(0,1,0)	(0,1,0)	(0,1,0)	(0,1,0)	(0,1,0)	(0,1,0)	(0,1,0)
λ_3 (10^{-3} GPa^{-1})	-0.7(3)	0.09(24)	0.84(25)	1.3(3)	1.6(3)	1.8(3)	1.9(3)	2.1(3)	2.2(5)
ev_3 (λ_3)	(0.33,0,0.94)	(0.34,0,0.94)	(0.34,0,0.94)	(0.34,0,0.94)	(0.33,0,0.94)	(0.32,0,0.95)	(0.31,0,0.95)	(0.27,0,0.96)	(0.22,0,0.98)
Ψ, θ(°)[a]	109.1(3), 0.8(3)	110.1(3), -0.7(3)	110.1(4), -1.1(4)	109.7(5), -1.0(5)	109.3(6), -0.8(6)	108.7(7), -0.4(7)	108.0(8), 0.2(8)	105.8(1.1), 2.2(1.1)	102.6(2.6), 5.2(2.6)

[a] The direction of maximum compressibility is located at the (0 1 0) plane at the given angles Ψ to the *c*-axis (from *c* to *a*) and θ to the *a*-axis (from *a* to *c*).

Table 2. Theoretical isothermal compressibility tensor coefficients, β_{ij}, for As_2S_3 and their respective eigenvalues, λ_i, and eigenvectors, ev_i, at different pressures. The results are obtained by employing the finite Eulerian method. The eigenvalues are given in decreasing value along a column.

P(GPa)	0.0	1.0	2.0	3.0	4.0	5.0	6.0	8.0	10.0
β_{11} (10^{-3} GPa^{-1})	40.0(2.2)	27.4(1.4)	20.1(1.4)	16.1(1.2)	13.5(1.0)	11.7(8)	10.3(8)	8.3(6)	7.0(6)
β_{22} (10^{-3} GPa^{-1})	25.8(1.4)	19.4(1.0)	15.0(1.1)	12.2(0.9)	10.3(7)	9.0(6)	7.9(6)	6.4(5)	5.4(4)
β_{33} (10^{-3} GPa^{-1})	3.58(24)	3.49(21)	3.4(3)	3.3(0.3)	3.2(3)	3.1(3)	3.07(24)	2.93(24)	2.8(3)
β_{13} (10^{-3} GPa^{-1})	-13.9(7)	-10.2(5)	-7.3(5)	-5.4(0.4)	-4.2(3)	-3.25(24)	-2.60(20)	-1.80(15)	-1.36(17)
λ_1 (10^{-3} GPa^{-1})	44.7(2.4)	31.1(1.6)	22.8(1.6)	18.1(1.3)	15.0(1.1)	12.8(9)	11.2(8)	8.9(7)	7.4(7)
ev_1 (λ_1)	(0.95,0,-0.32)	(0.94,0,-0.35)	(0.94,0,-0.35)	(0.94,0,-0.35)	(0.94,0,-0.33)	(0.95,0,-0.32)	(0.95,0,-0.31)	(0.96,0,-0.29)	(0.96,0,-0.28)
λ_2 (10^{-3} GPa^{-1})	25.8(1.3)	19.4(1.0)	15.0(1.1)	12.2(0.9)	10.3(7)	9.0(6)	7.9(6)	6.3(5)	5.4(4)
ev_2 (λ_2)	(0,1,0)	(0,1,0)	(0,1,0)	(0,1,0)	(0,1,0)	(0,1,0)	(0,1,0)	(0,1,0)	(0,1,0)
λ_3 (10^{-3} GPa^{-1})	-1.14(15)	-0.27(0.13)	0.67(13)	1.31(16)	1.76(18)	2.05(19)	2.23(20)	2.39(21)	2.4(3)
ev_3 (λ_3)	(0.32,0,0.95)	(0.35,0,0.94)	(0.35,0,0.94)	(0.35,0,0.94)	(0.33,0,0.94)	(0.32,0,0.95)	(0.31,0,0.95)	(0.29,0,0.96)	(0.28,0,0.96)
Ψ, θ(°)[a]	108.73(20), 1.12(20)	110.25(20), -1.03(20)	110.56(20), -1.84(20)	110.2(3), -1.9(3)	109.5(4), -1.4(4)	108.6(4), -0.8(4)	107.9(5), -0.2(5)	106.8(7), 0.6(7)	106.5(1.7), 0.7(1.7)

[a] The direction of maximum compressibility is located at the *ac* plane; i.e. the (0 1 0) plane, at the given angle Ψ to the *c*-axis (from *c* to *a*) and θ to the *a*-axis (from *a* to *c*).

P(GPa)	14.3	17.4	18.8	20.4	22.2	24.3[b]	26.7	29.3	32.0
β_{11} (10^{-3} GPa^{-1})	5.57 (21)	5.4(8)	5.2(7)	4.5(6)	2.8(5)	2.0(4)	1.8(4)	1.7(3)	1.6(3)
β_{22} (10^{-3} GPa^{-1})	4.11 (13)	3.5(4)	3.4(4)	3.3(3)	2.90(24)	2.82(21)	2.52(18)	2.26(16)	2.00(14)
β_{33} (10^{-3} GPa^{-1})	2.53(9)	2.2(4)	1.9(4)	1.7(3)	2.2(3)	2.4(3)	2.40(24)	2.37(23)	2.32(21)
β_{13} (10^{-3} GPa^{-1})	-0.86(4)	-0.77(16)	-0.65(14)	-0.23(12)	0.46(10)	0.38(9)	0.30(8)	0.19(7)	0.20(20)
λ_1 (10^{-3} GPa^{-1})	5.80(22)	5.5(8)	5.3(8)	4.6(6)	3.0(4)	2.82(21)	2.52(18)	2.42(23)	2.37(21)
ev_1 (λ_1)	(0.97,0,-0.25)	(0.97,0,-0.23)	(0.98,0,-0.19)	(1.00,0,-0.08)	(0.87,0,0.49)	(0,1,0)	(0.38,0,0.93)	(0.26,0,0.97)	(0.26,0,0.97)
λ_2 (10^{-3} GPa^{-1})	4.11(13)	3.5(4)	3.4(4)	3.3(3)	2.90(24)	2.6(3)	2.52(18)	2.26(16)	2.00(14)
ev_2 (λ_2)	(0,1,0)	(0,1,0)	(0,1,0)	(0,1,0)	(0,1,0)	(0.55,0,0.84)	(0,1,0)	(0,1,0)	(0,1,0)
λ_3 (10^{-3} GPa^{-1})	2.30(9)	2.0(4)	1.8(4)	1.7(3)	2.0(3)	1.8(3)	1.7(3)	1.7(3)	1.6(3)
ev_3 (λ_3)	(0.25,0,0.97)	(0.23,0,0.97)	(0.19,0,0.98)	(0.08,0,1.00)	(0.49,0,-0.87)	(0.84,0,-0.55)	(0.93,0,-0.38)	(0.97,0,-0.26)	(0.97,0,-0.26)
Ψ, θ(°)[a]	104.8(6), 2.3(6)	103.1(1.8), 3.8(1.8)	101.1(1.6), 5.8(1.6)	94.7(1.8), 12.2(1.8)	61(13), 46(13)		22.0(1), 85.1(1)	15(5), 92(5)	15(4), 92(4)

[a] The direction of maximum compressibility is located at the *ac* plane; i.e. the (0 1 0) plane, at the given angle Ψ to the *c*-axis (from *c* to *a*) and θ to the *a*-axis (from *a* to *c*).

[b] At 24.3 GPa, the direction of maximum compressibility is along *b*-axis; i.e. the [010] direction.

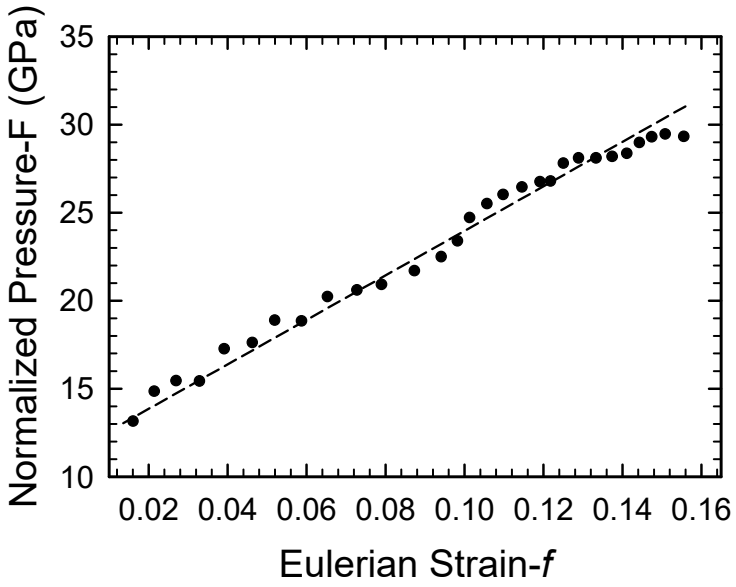

Figure S15. Normalized pressure vs Eulerian strain (F-f plot).

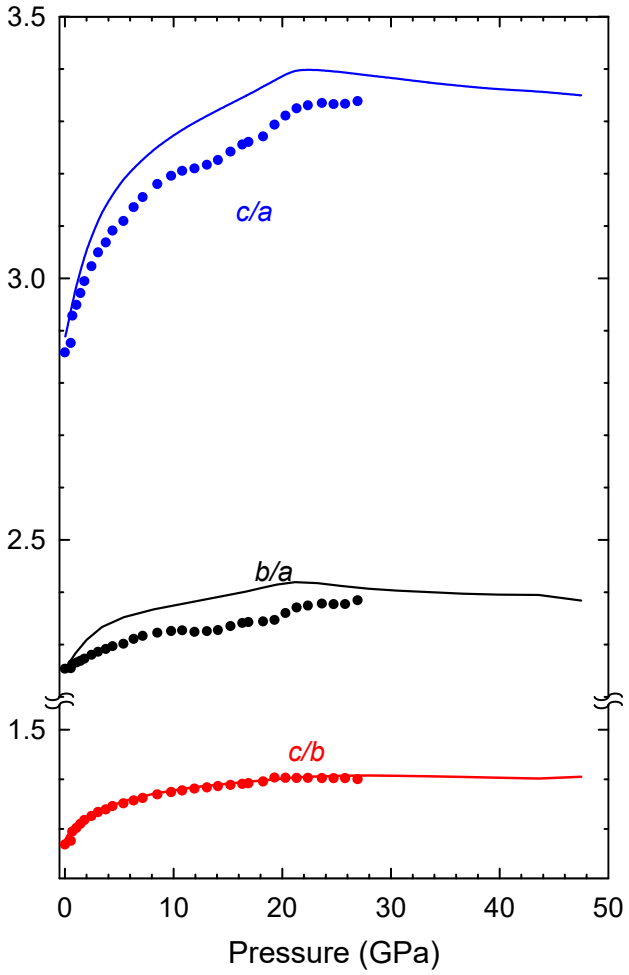

Figure S16. Pressure dependence of the experimental (symbols) and theoretical (lines) lattice parameter ratios as a function of pressure. Theoretical calculations include vdW dispersion corrections.

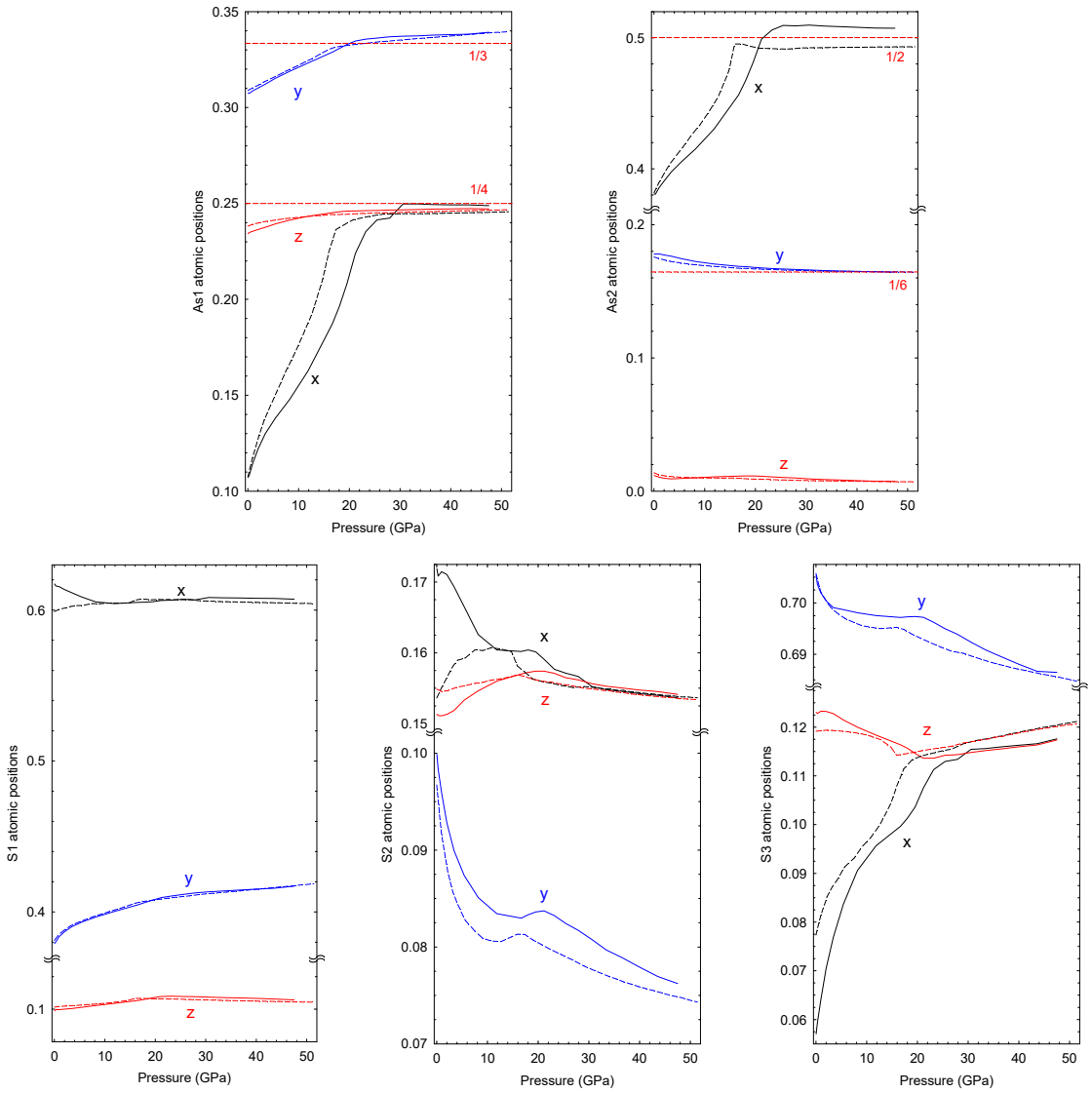

Figure S17. Pressure dependence of the theoretical free coordinates belonging to the different Wyckoff sites of the α-As_2S_3. Calculations with (without) vdW interactions are depicted as solid (dashed) lines. Compared to the As atomic coordinates, the S atomic coordinates show a very complex tendency with pressure. However, all of these show considerable changes above 18 and 25 GPa for calculations that do not consider and consider vdW interactions, respectively. Curiously, the erratic behavior of the S atomic coordinates is not reflected in the smooth HP dependence of the As-S interatomic distances (see Figure 6 in the main paper) that are mainly dominated by the strong changes of the x coordinate of As atoms.

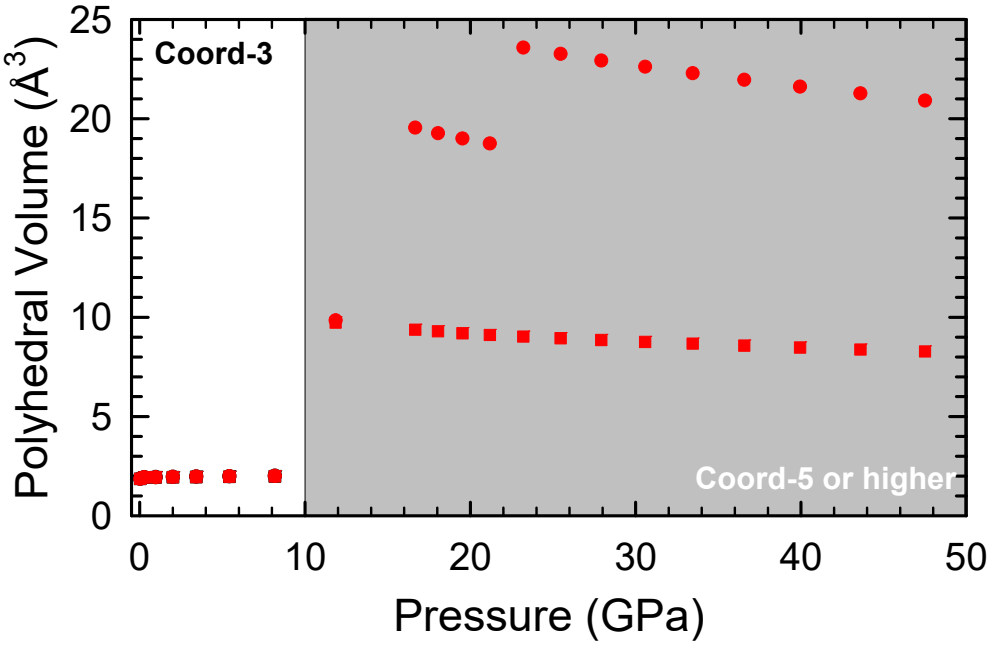

Figure S18. Pressure dependence of the theoretically predicted polyhedral unit volume around As1 (circles) and As2 (squares).

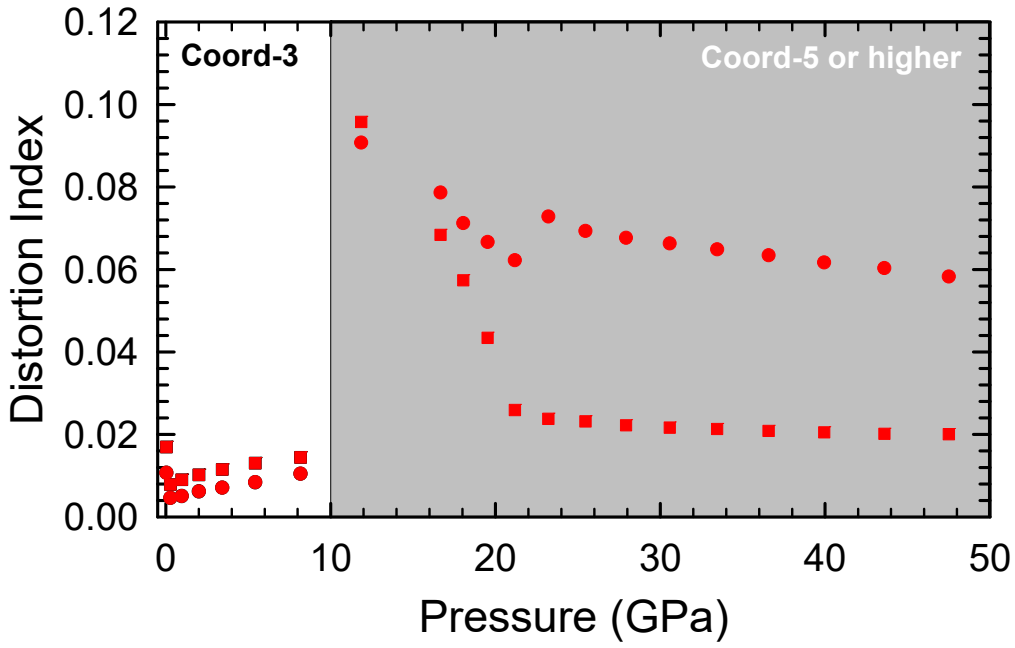

Figure S19. Pressure dependence of the theoretically predicted distortion index of the polyhedral units around As1 (circles) and As2 (squares).

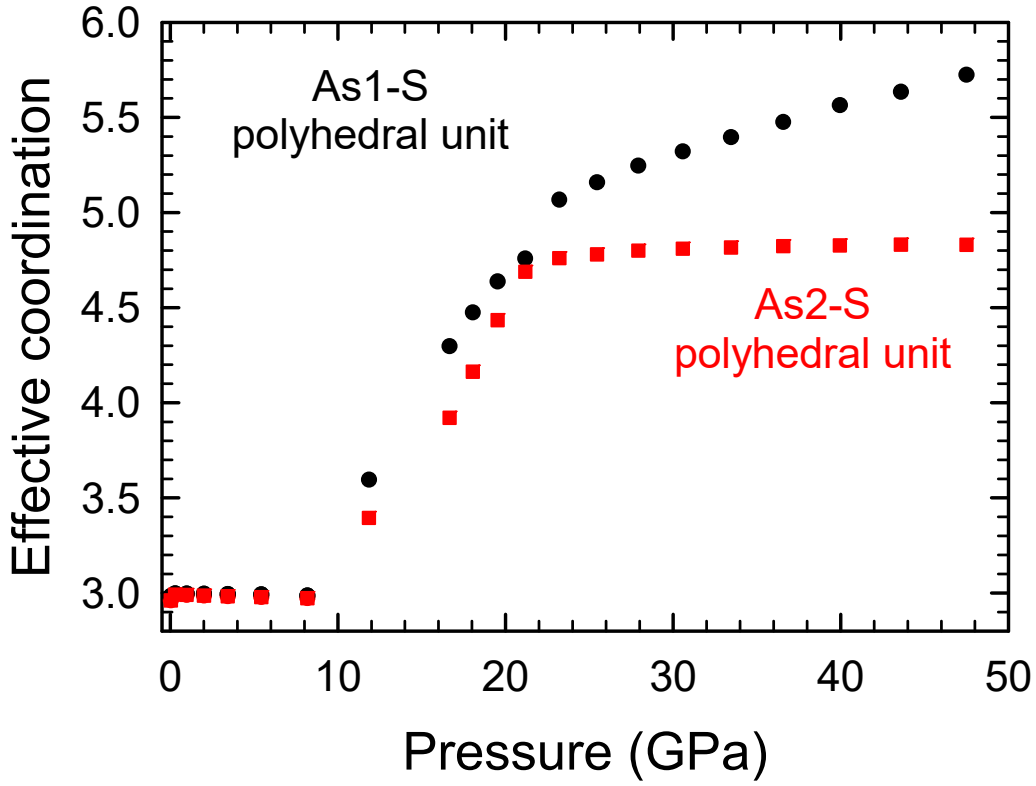

Figure S20. Pressure dependence of the theoretically predicted effective coordination number of polyhedral units around As1 (circles) and As2 (squares). Effective coordination number is calculated according to Ref. **[7]**.

Vibrational properties of orpiment under compression

In layered compounds with typical van der Waals gap between the layers, the low-frequency inter-layer shear mode exhibits a much smaller pressure coefficient than other modes, whereas the low-frequency A (or B) mode displays the largest pressure coefficient. For example, the E and A modes with frequencies around 40 (60) cm^{-1} and 116 (133) cm^{-1} in InSe (GaSe) have pressure coefficients of 0.68 (0.85) cm^{-1}/GPa and 5.41 (5.78) cm^{-1}/GPa, respectively **[8,9]**. Similar behavior is found for layered topological insulators Bi_2Se_3, Bi_2Te_3 and Sb_2Te_3 **[10-12]**.

Usually, the small pressure coefficient of the low-frequency E mode in layered materials is ascribed to the weak bending force constant due to weak van der Waals forces between the neighboring layers. On the other hand, the large pressure coefficient of the low-frequency A mode is due to the extraordinary increase of the stretching force constant between neighboring layers due to the strong decrease of the inter-layer distance **[8,9]**.

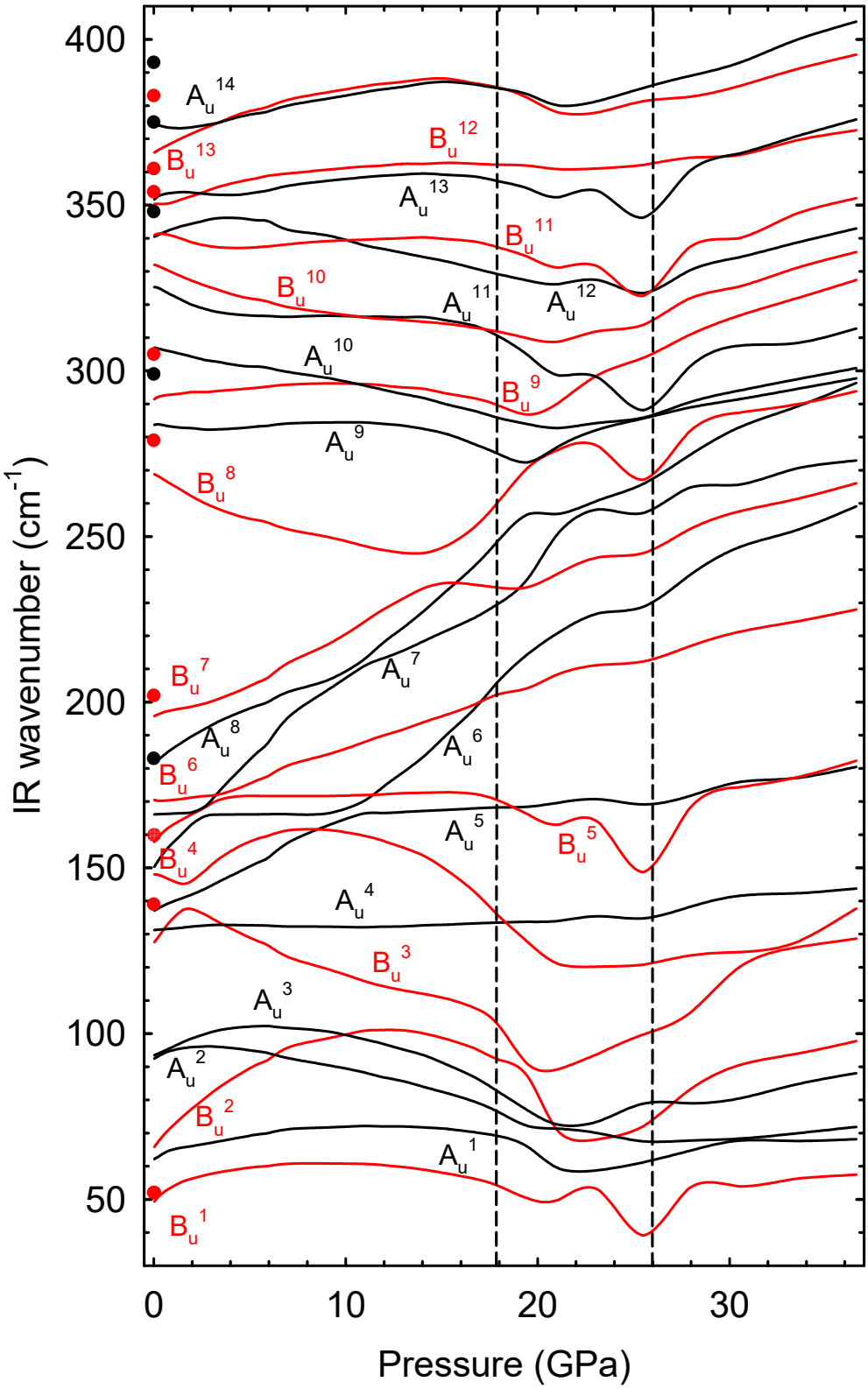

Figure S21. HP dependence of the theoretical wavenumbers of the IR-active modes in α-As_2S_3. Considerable softening of some vibrational modes is observed above 4 GPa and between 18 and 26 GPa. Experimental data at room pressure (symbols) from Ref. 14, 15 have been included.

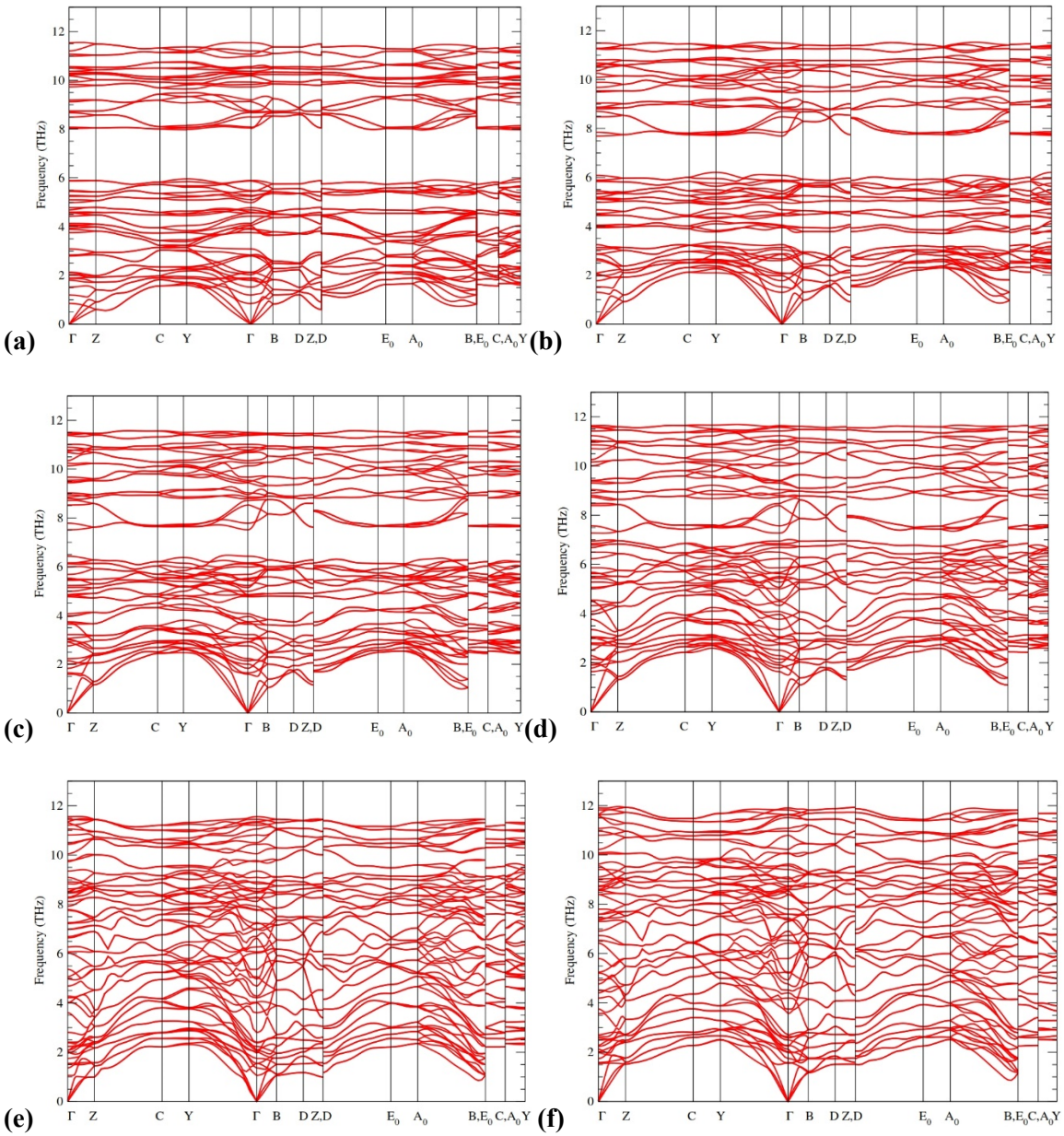

Figure S22. Calculated phonon dispersion curves of As_2S_3 at different pressures: **(a)** 0 GPa, **(b)** 5 GPa, **(c)** 10 GPa, **(d)** 15 GPa, **(e)** 21 GPa, and **(f)** 30 GPa.

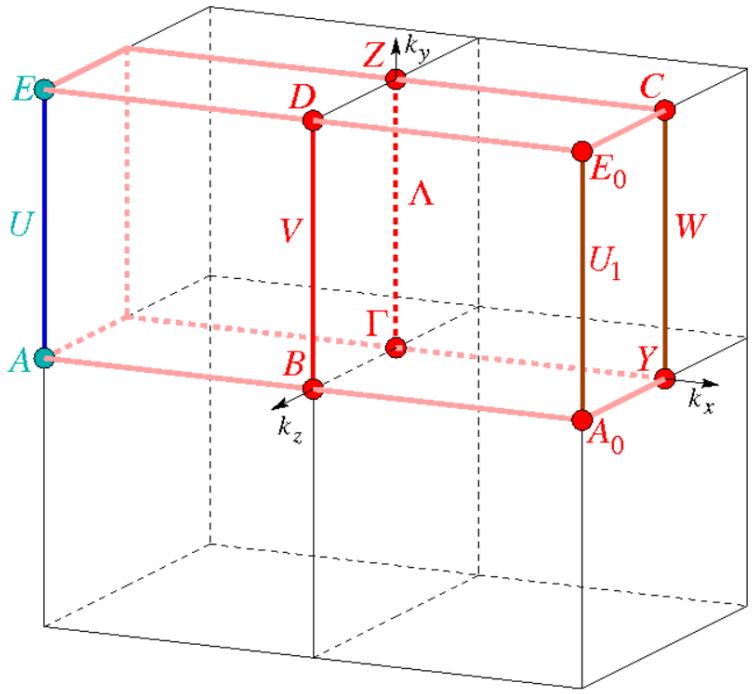

Figure S23. Representation of the points and paths used in the first Brillouin zone of monoclinic α-As_2S_3 in order to perform calculations of phonon dispersion curves and electronic band structures. Taken from the Bilbao Crystallographic Server database **[13]**.

Table S2. Theoretical (with vdW interactions) and experimental IR-active mode frequencies and their respective pressure coefficients for α-As_2S_3 at room temperature, as fitted with equation $\omega(P) = \omega_0 + \alpha \cdot P$. Experimental values have been added for comparison.

	Theoretical		Experimental
Mode (Sym)	$\omega_0\ (cm^{-1})$ [a]	$\alpha\ \left(\frac{cm^{-1}}{GPa}\right)$ [a]	$\omega_0\ (cm^{-1})$
B_u^1	50 (1)	4.3 (3)	52 [c]
A_u^1	63 (1)	2.3 (3)	
B_u^2	66 (1)	6.5 (2)	
A_u^2	93 (1)	2.5 (2)	
A_u^3	94 (1)	3.2 (1)	
B_u^3	128 (2)	8 (1)	
A_u^4	131 (2)	0.7 (1)	
A_u^5	137 (2)	2.3 (1)	
B_u^4	148 (2)	-2.5 (9)	140 [b], 139 [c]
A_u^6	150 (2)	8.8 (3)	
B_u^5	158 (2)	5.2 (3)	159 [b], 160 [c]
A_u^7	167 (2)	-1.8 (4)	
B_u^6	170 (2)	-0.1 (2)	
A_u^8	182 (2)	4.6 (1)	181 [b], 183 [c]
B_u^7	196 (2)	1.1 (2)	198 [b], 202 [c]
B_u^8	269 (3)	-4.0 (1)	279 [b]
A_u^9	284 (3)	-1.0 (1)	299 [b]
B_u^9	292 (3)	1.1 (2)	311 [b], 305 [c]
A_u^{10}	307 (4)	-1.6 (1)	
A_u^{11}	326 (4)	-3.5 (2)	345 [b], 348 [c]
B_u^{10}	332 (4)	-2.8 (1)	354 [b,c]
A_u^{12}	340 (4)	2.7 (1)	
B_u^{11}	342 (4)	-1.7 (4)	
B_u^{12}	350 (4)	1.2 (3)	361 [c]
A_u^{13}	352 (4)	1.2 (4)	375 [b]
B_u^{13}	366 (4)	3.1 (1)	383 [b], 381 [c]
A_u^{14}	374 (4)	-1.0 (1)	393 [c]

[a] This work. [b] Ref. 14. [c] Ref. 15.

Table S3. Known crystalline phases of group-15 A_2B_3 sesquichalcogenides at room pressure, their space groups, stability at room pressure, average cation coordination and bonding type.

Compound	Space group	Stability at room pressure	Average cation coordination	Bonding-type
α-As_2S_3	*P2₁/c*	Stable	3	p-type covalent
α-As_2Se_3	*P2₁/c*	Stable	3	p-type covalent
β-As_2Se_3	*C2/m*	Metastable	3	p-type covalent
γ-As_2Se_3	*R-3m*	Metastable	6	metavalent
α-As_2Te_3	*C2/m*	Stable	5.5	mixed*
β-As_2Te_3	*R-3m*	Metastable	6	metavalent
α-Sb_2S_3	*Pnma*	Stable	4	mixed*
α-Sb_2Se_3	*Pnma*	Stable	4	mixed*
α-Sb_2Te_3	*R-3m*	Stable	6	metavalent
α-Bi_2S_3	*Pnma*	Stable	4	mixed*
α-Bi_2Se_3	*R-3m*	Stable	6	metavalent
α-Bi_2Te_3	*R-3m*	Stable	6	metavalent

* It is a mixture between p-type covalent and metavalent

Possible high pressure phase

Above 42 GPa, Liu and co-workers **[16]** found a possible 1st order phase transition by a drastic decrease of the electrical resistivity above this pressure. This feature was assigned to a pressure-induced metallization but there was not identification of the high pressure phase. We do not want to finish the full picture of the behaviour of orpiment under compression without providing a hint of this possible high pressure phase. According to our *ab initio* theoretical simulations above 40 GPa, we found a new structure competitive with the low pressure phase (see **Figure S24**).

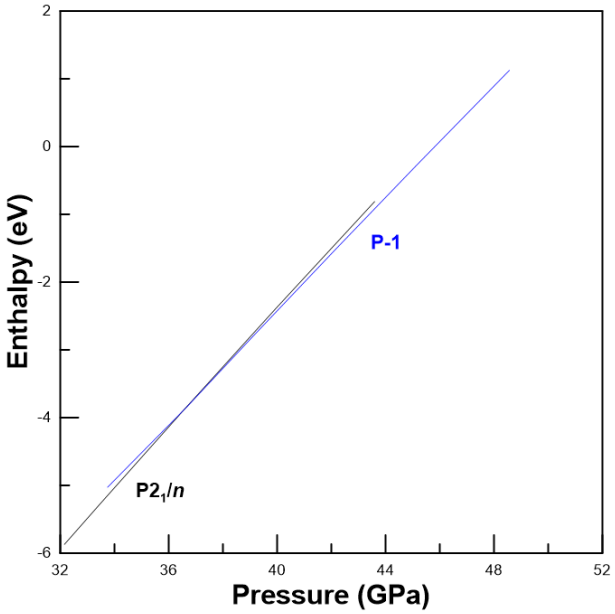

Figure S24. Enthalpy vs pressure around 40 GPa of low pressure phase (*P2₁/n*) and a proposed high pressure phase (*P-1*).

Le Bail fittings at different pressures

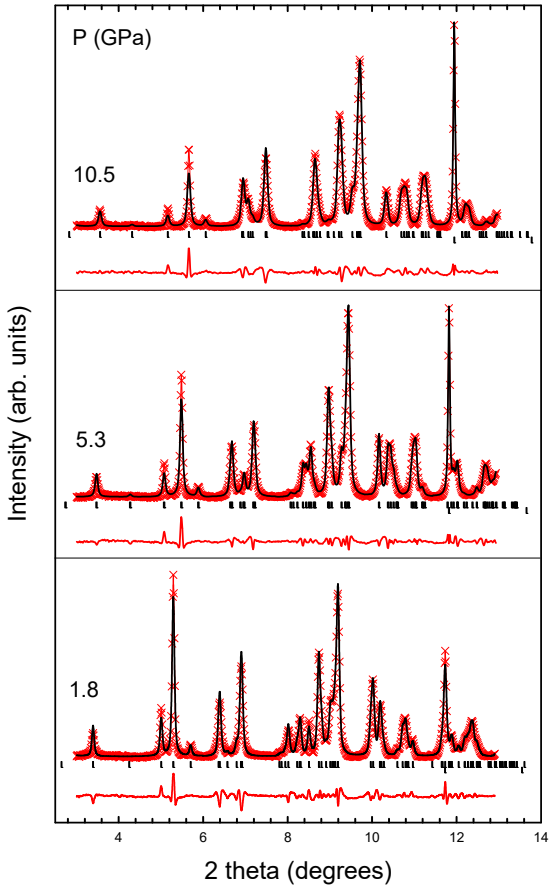

Figure S25. Le Bail fitting (black line) of the experimental X-ray diffraction pattern (red cross) at several pressures (1.8, 5.3 and 10.5 GPa) together with the residual curve (red line). Vertical ticks indicate the Cu (bottom) and α-As_2S_3 (top) Bragg reflections.

References

(1) Mullen, D.J.E.; and Nowacki, W. Refinement of the crystal structures of realgar, AsS and orpiment, As_2S_3. *Z. Kristall.* **1972**, 136, 48.

(2) Defonzo, A.P.; and Tauc, J. Network dynamics of 3:2 coordinated compounds. *Phys. Rev. B* **1978**, 18, 6957.

(3) Zallen, R.; and Slade, M. Rigid-layer modes in chalcogenide crystals. *Phys. Rev. B* **1974**, 9, 1627.

(4) Canepa, R.; Hanson, R. M.; Ugliengo, P.; Alfredsson, M. J-ICE: a new Jmol interface for handling and visualizing crystallographic and electronic properties. *J. Appl. Cryst.* **2011**, 44, 225-229.

(5) Haussühl, S. Physical Properties of Crystals. An Introduction (Wiley-VCH, Weinheim, 2007).

(6) Angel, R. J. http://www.rossangel.com/text_strain.htm

(7) Hoppe, R. Effective coordination numbers (ECoN) and mean Active fictive ionic radii (MEFIR). *Z. Kristall.* **1979**, 150, 23.

(8) Ulrich, C.; Mroginski, M.; Goñi, A.R.; Cantarero, A.; Schwarz, U.; Muñoz, V.; and Syassen, K. Vibrational Properties of InSe under Pressure: Experiment and Theory. *Phys. Stat. Sol. (b)* **1996**, 198, 121.

(9) Kulibekov, A.M.; Olijnyk, H. P.; Jephcoat, A. P.; Salaeva, Z. Y.; Onari, S.; and Allakverdiev, K.R. Raman Scattering under Pressure and the Phase Transition in ε-GaSe. *Phys. Stat. Sol (b)* **2003**, 235, 517.

(10) Vilaplana, R.; Gomis, O.; Manjón, F.J.; Segura, A.; Pérez-González, E.; Rodríguez-Hernández, P.; Muñoz, A.; González, J.; Marín-Borrás, V.; Muñoz-Sanjosé, V.; Drasar, C.; and Kucek, V. High-Pressure Vibrational and Optical Study of Bi2Te3. *Phys. Rev. B* **2011**, 84, 104112.

(11) Gomis, O.; Vilaplana, R.; Manjón, F.J.; Rodríguez-Hernández, P.; Pérez-González, E.; Muñoz, A.; Kucek, V.; and Drasar, C. Lattice Dynamics of Sb2Te3 at High Pressures. *Phys. Rev. B* **2011**, 84, 174305.

(12) Vilaplana, R.; Santamaría-Pérez, D.; Gomis, O.; Manjón, F.J.; González, J.; Segura, A.; Muñoz, A.; Rodríguez-Hernández, P.; Pérez-González, E.; Marín-Borrás, V.; Muñoz-Sanjosé, V.; Drasar, C.; Kucek, V. Structural and Vibrational Study of Bi2Se3 under High Pressure. *Phys. Rev. B* **2011**, 84, 184110.

(13) Aroyo, M. I.; Orobengoa, D.; de la Flor, G.; Tasci, E. S.; Perez-Mato, J. M.; Wondratschek, H. Brillouin-zone database on the Bilbao Crystallographic Server. *Acta Cryst.* **2014**, A70.

(14) Zallen, R.; Slade, M.; Ward, A.T. Lattice vibrations and Interlayer Interactions in Crystalline As_2S_3 and As_2Se_3. *Phys. Rev. B* **1971**, 3, 4257.

(15) Forneris, R. The infrared and Raman spectra of realgar and orpiment. *Am. Miner.* **1969**, 54, 1062.

(16) Liu, K. X.; Dai, L. D.; Li, H. P.; Hu, H. Y.; Yang, L. F.; Pu, C.; Hong, M. L.; Liu, P.F. Phase Transition and Metallization of Orpiment by Raman Spectroscopy, Electrical Conductivity and Theoretical Calculation under High Pressure. *Materials* **2019**, 12, 784.